Received: 19 August 2024 | Revised: 15 January 2025 | Accepted: 20 March 2025

DOI: 10.1002/mawe.202400249

ARTICLE

WILEY VCH

Investigation of hot ductility behavior of micro-alloyed steel and the effect of strain rate and dynamic phase transformation on the 2nd ductility minimum

Untersuchung des Warmduktilitätsverhaltens von mikrolegiertem Stahl und des Einflusses der Dehnungsrate und der dynamischen Phasenumwandlung auf das zweite Duktilitätsminimum

S. Bakhtiari[1,2] | S. S. Sharifi[2] | S. Ilie[3] | C. Sommitsch[2]

[1]K1-MET GmbH, Linz, Austria

[2]Institute of Materials Science, Joining and Forming at the Graz University of Technology, Graz, Austria

[3]Voestalpine Stahl GmbH, Linz, Austria

Correspondence
S. Bakhtiari, K1-MET GmbH, Stahlstraße 14, 4020 Linz, Austria.
Email: saeid.bakhtiari@k1-met.com

Funding information
COMET program, Grant/Award Number: FO999892415

Abstract

Continuous casting of steel is widely used to manufacture semi-finished long or flat products. Various stresses are present during slab casting: stresses arise from friction between the mold wall and the solidified shell, thermal stresses on the strand surface, and stresses from bending and straightening operations. Steels present a minimum ductility point during continuous casting in the solid-state condition. This work aims to answer the metallurgical reasons for the occurrence of the ductility minimum in a micro-alloyed steel by investigating the microstructural evolution. The samples are in situ melted via induction heating in the BETA250-5® thermomechanical simulator machine, followed by hot tensile tests conducted at different temperatures and strain rates. The ductility drop is analyzed in the range of 650 °C–1100 °C at different strain rates, $10^{-2}\,s^{-1}$ to $10^{-3}\,s^{-1}$. Furthermore, the study investigated the development of the ferrite phase at the prior austenite grain boundaries, the thickness of ferrite, dynamic phase transformation, and the influence of the test conditions on these parameters. The fracture mechanism and ferrite phase thickness are determined from metallography investigations using light optical microscopy and scanning electron microscopy. Finally, the microstructural changes are correlated to the ductility minimum using the measured results.

KEYWORDS
continuous casting, ductility minimum, hot ductility, micro-alloyed, steel

SCHLÜSSELWÖRTER
mikrolegiert, Mindestduktilität, Stahl, Strangguss, Warmduktilität

1 | INTRODUCTION

Continuous casting is the primary method for producing steel in semi-finished forms like slabs, blooms, and billets. Nowadays, approximately 96.8 % of total steel production uses continuous casting. This method is favored for its high efficiency, large capacity, and low energy consumption, introducing its widespread application [1, 2]. In this process, molten steel is poured from a ladle into a tundish. From the tundish, the steel flows into a hollow, water-cooled copper mold. As the molten steel enters the mold, it begins to solidify and forms a shell in contact with the mold. The steel is then continuously pulled out from the bottom of the mold [3, 4]. During solidification and straightening, the product experiences mechanical forces such as ferrostatic pressure exerted by the molten material on the shell, casting weight, bending force, mold friction, roll cage misalignment, and thermal stresses due to uneven cooling in secondary cooling zone [3–5]. The interacting stresses impact mechanical properties, specifically formability, of the product. These stresses result in overall tensile stress on the surface of the product, leading to crack initiation, either on the surface or within the product, posing a risk of steel slab failure. Fracture in the solidifying shell can occur in various forms, from complete failure to partial surface or internal defects, particularly transverse corner cracks. These cracks are more likely to be initiated in areas where the material exhibits minimum ductility [3, 5, 6].

As the predominant stress on the casting strand after bending and straightening is tensile, conducting a hot tensile test is the most suitable approach for simulating the process and addressing the relationship between ductility and crack initiation on a laboratory scale [7]. Researchers establish the relationship between the tensile test and steel ductility by examining the reduction in area following the tensile test. This examination helps correlate ductility with crack formation susceptibility [8–12]. Plotting the reduction in area versus temperature reveals a trough in the curve, typically occurring between 700 °C and 1000 °C. This range varies depending on the chemical composition and test conditions. Known as the second ductility minimum of steel, this trough helps predict the likelihood of transverse corner cracks in the strand. Crack formation occurs when the steel‘s ductility falls below a critical threshold, specifically when the reduction in area drops below 40 %, indicating brittle fracture of the sample [2, 5, 7, 13–16].

Preventing or minimizing crack formation is crucial for improving slab quality and reducing production costs, which can be achieved through enhanced hot ductility. Factors influencing hot ductility include the formation of ferrite films and impurity segregation at primary austenite grain boundaries, as well as the presence of precipitates such as carbides or nitrides of vanadium, titanium, or niobium at grain boundaries, and microstructural changes like dynamic recrystallization during straightening at elevated temperatures [17, 18].

Investigations demonstrated that a thin ferrite film formed at grain boundaries can enhance intergranular failure, attributing this to higher dynamic recovery in ferrite compared to austenite, leading to strain concentration and promoting void nucleation and crack initiation [5]. Furthermore, the study of the hot ductility behavior of chromium-molybdenum steel shows that deformation-induced ferrite at grain boundaries reduces ductility, causing intergranular fractures [19].

The presence of precipitates induces local hardening and stress concentration, further impairing ductility [5, 20, 21]. Research on investigation of hot ductility of titanium-niobium micro-alloyed steels through various thermal histories shows that the presence of small and finely dispersed titanium-niobium rich carbides can reduce the ductility of the titanium-niobium steel [20]. Alloying elements like manganese, titanium, boron, aluminum, and vanadium can promote precipitation. When combined with the ferrite films formed at grain boundaries during phase transformation, these elements can contribute to crack initiation [22].

Some investigations depict that in niobium-containing steels, precipitates form in the austenite during deformation, with grain boundary precipitation leading to the formation of precipitate-free zones that encourage void formation [5]. The study on the influence of nitride precipitates on crack formation shows that fracture occurs due to cavity coalescence at grain boundary precipitates. It is concluded that the presence of strong nitride formers such as aluminum, niobium and boron in excess to critical concentrations reduces the ductility [18].

Apart from these factors, strain rate significantly influences steel ductility. Studies show that increasing strain rate enhances the hot ductility behavior of micro-alloyed steels [5, 14, 23–27]. The investigation of the effect of deformation speed on the formation of deformation-induced ferrite and the softening behavior of this phase revealed that deformation speed impacts the thickness of ferrite, which subsequently alters the strain concentration and, thereby, the ductility of the specimens [28]. Additionally, studies on the influence of strain rate and dynamic recrystallization on the hot ductility of low carbon steel show that high strain rates reduce grain boundary sliding, thereby, improving the ductility. Additionally, it is reported that dynamic recrystallization must be well advance to be effective in improving the ductility [29]. Furthermore, recent work

TABLE 1 Chemical composition of the studied material measured by optical emission spectrometry [wt.–%].

Carbon	Chromium	Manganese	Aluminium	Nitrogen	Silicon	Sulfur	Phosphorus
0.09	0.28	1.92	0.06	52 ppm	0.15	50 ppm	90 ppm

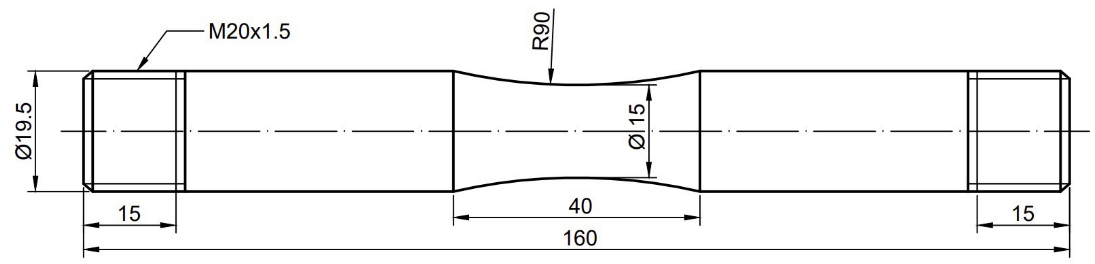

FIGURE 1 Geometry of the dog-bone shaped tensile testing sample. Dimensions are in mm [10].

investigated the influence of thermomechanical conditions, such as temperature and strain rate, on the microstructural changes of microalloyed steel in both single-phase and two-phase domains using a mesoscale model [30]. We found that, in addition to dynamic recrystallization, dynamic phase transformation under different deformation speeds affects the mechanical properties of the material. This impact occurs by changing the hardening and softening behavior of the phases due to the evolving strain rate caused by the variation in the ferrite fraction.

This study assesses the hot ductility behavior of a low carbon microalloyed steel using hot tensile tests on in situ melted samples at different temperatures and strain rates. The investigation examines not only ductility behavior but also changes in the fractured surface, microstructure, and the influence of the ferrite thickness on the ductility trough.

2 | EXPERIMENTAL AND MATERIALS

The low carbon microalloyed steel used in the experiments was provided by Voestalpine Stahl GmbH, Table 1. Cylindrical dog-bone shaped samples were machined from slabs obtained through continuous casting, with their axes aligned parallel to the rolling direction, Figure 1 [10].

An in-house thermomechanical simulator, BETA 250–5, equipped with a vacuum chamber was used for the performance of the hot tensile tests. The tensile test unit delivered by Messphysik, Fürstenfeld, Austria, which was rebuilt from mechanical testing systems (MTS), Eden Prairie, United States. Further improvements regarding the design of the induction coil, cooling system, and data acquisition, were made at Graz University of Technology, Figure 2 [10].

The tension arm of the device holds the upper part of the specimen and controls the vertical displacement, whereas the lower part is fixed. The lower part is supported by a spring and three gripper arms that accommodate thermal expansion during the test. To control the surface temperature, a pair of type *S* (platinum/platinum-rhodium) thermocouples were spot-welded in the middle of the sample. To achieve in-situ melting the specimen was heated such that inside the specimen reached the melting temperature, while the measured temperature at the surface was around 1440 °C. By

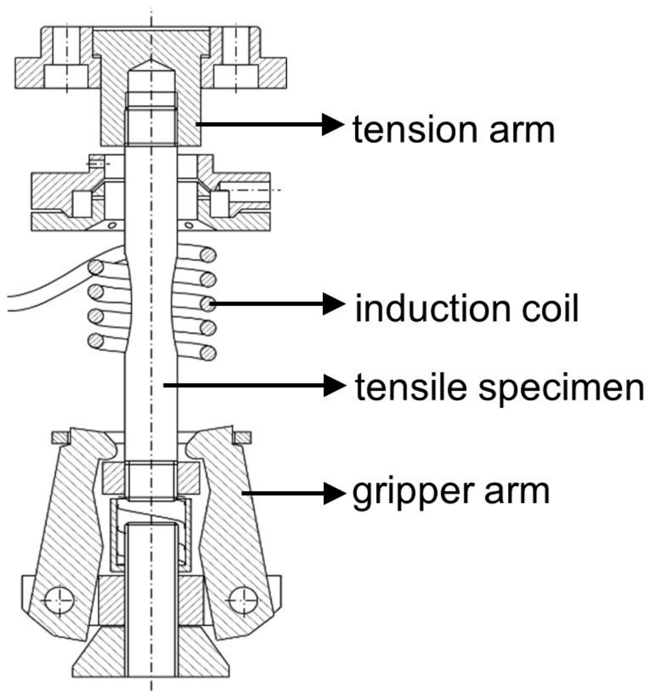

FIGURE 2 Schematic of tensile testing setup in BETA 250–5 simulator, modified after [10].

controlling the heat input and the pressure inside the chamber, around 0.3 mbar, a stable thin oxide layer (30 μm–40 μm) was formed to prevent the molten steel from spilling.

The induction coil was connected to the upper part of the machine and moved upwards at half speed of the upper arm during the tensile test to ensure the heating remained concentrated in the center of the specimen. The specimens were soaked at the highest temperature for 15 s before cooling to the test temperature. After soaking, the specimens were cooled down to 1300 °C at a cooling rate of 5 °C s^{-1}. The cooling rate from 1300 °C to the deformation temperatures (650 °C–1100 °C) was 1 °C s^{-1}. The specimens were held for 10 s before the start of the hot tensile test, which was performed with the strain rates of 10^{-2} s^{-1} and 10^{-3} s^{-1} until the rupture. The thermomechanical conditions, including temperature, cooling rate, and strain rate were selected to closely match those of industrial operations, Figure 3 [7, 23, 24].

Finally, the area of the fractured surface was optically measured with a Zeiss stereo microscope, model Discovery V20 (Oberkochen, Germany). The reduction in area can be calculated using the measured fracture surface, *Equation (1)*.

$$\%\,RA = \left(\frac{A_0 - A_f}{A_0}\right) \times 100 \tag{1}$$

where RA, A_0 and A_f are the reduction in area, the initial cross section area and the measured surface area after fracture, respectively. Moreover, the fracture surfaces were observed with a TESCAN Mira3 field emission scanning electron microscope (Dortmund, Germany) for the analysis and comparison of the failure mechanisms. The microstructure of the specimens is studied using an axio observer inverted light optical microscope from Zeiss (Oberkochen, Germany). For microstructural observations the fractured specimens were sectioned longitudinally. The cut surface was mechanically ground with silicon carbide papers up to P1200 and polished in two steps. First, for 5 minutes with an alumina suspension with 1 μm of particle size and 15 minutes with a colloidal silica suspension. The polished surface was etched using 3 % nital to identify ferrite phase and transformed austenite. ImageJ software was used to identify and quantify the ferritic thickness, two images were analyzed, and the results are an average of at least six measurements per image.

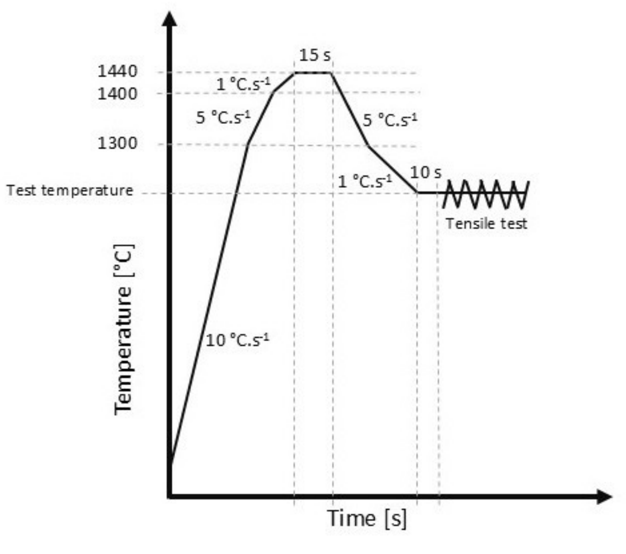

FIGURE 3 Thermomechanical path of hot tensile test using BETA 250–5.

3 | RESULTS

To plot the reduction in area for the specimens deformed at different temperatures in the range of 650 °C to 1100 °C and at the strain rates of 10^{-2} s^{-1} and 10^{-3} s^{-1}, the reduction in area value is the average of at least two specimens for each condition, Figure 4. The horizontal dashed line depicts the critical reduction in area of 40 % proposed by other studies [8]. The reduction in area curves present the typical hot ductility behavior. The ductility is high at elevated temperatures (> 850 °C) and reduces as the temperature decreases to around austenite to ferrite transformation temperature. At both strain rates, the reduction in area increases at lower temperatures (< 750 °C), indicating recovery in ductility. The samples deformed at a higher strain rate, 10^{-2} s^{-1}, show higher reduction in area values, suggesting better hot ductility. The curves show the trough, i. e. ductility minimum, at 750 °C and 800 °C under the strain rates of 10^{-2} s^{-1} and 10^{-3} s^{-1}, respectively.

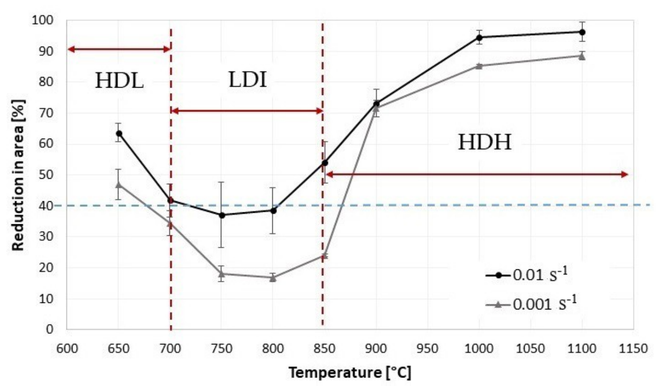

FIGURE 4 Reduction in area under different thermomechanical conditions.

The cross-sectional area in the scanning electron microscopy micrographs of the specimens strained to the rupture at different temperatures at the strain rate of $10^{-3}\ s^{-1}$, alters as temperature changes, Figure 5. At lowest temperature, the fracture surface contains microvoids and dimples suggesting ductile fracture, yellow arrows in Figure 5a. At intermediate temperatures, i.e. 700 °C–850 °C, the fracture surface comprises both brittle and ductile fracture characteristics, with brittleness being more pronounced at 750 °C and 800 °C, consistent with the calculated reduction in area, Figure 5b–e. Beyond 850 °C, the fracture surfaces again show dimples and microvoids, indicating ductile fracture, yellow arrows in

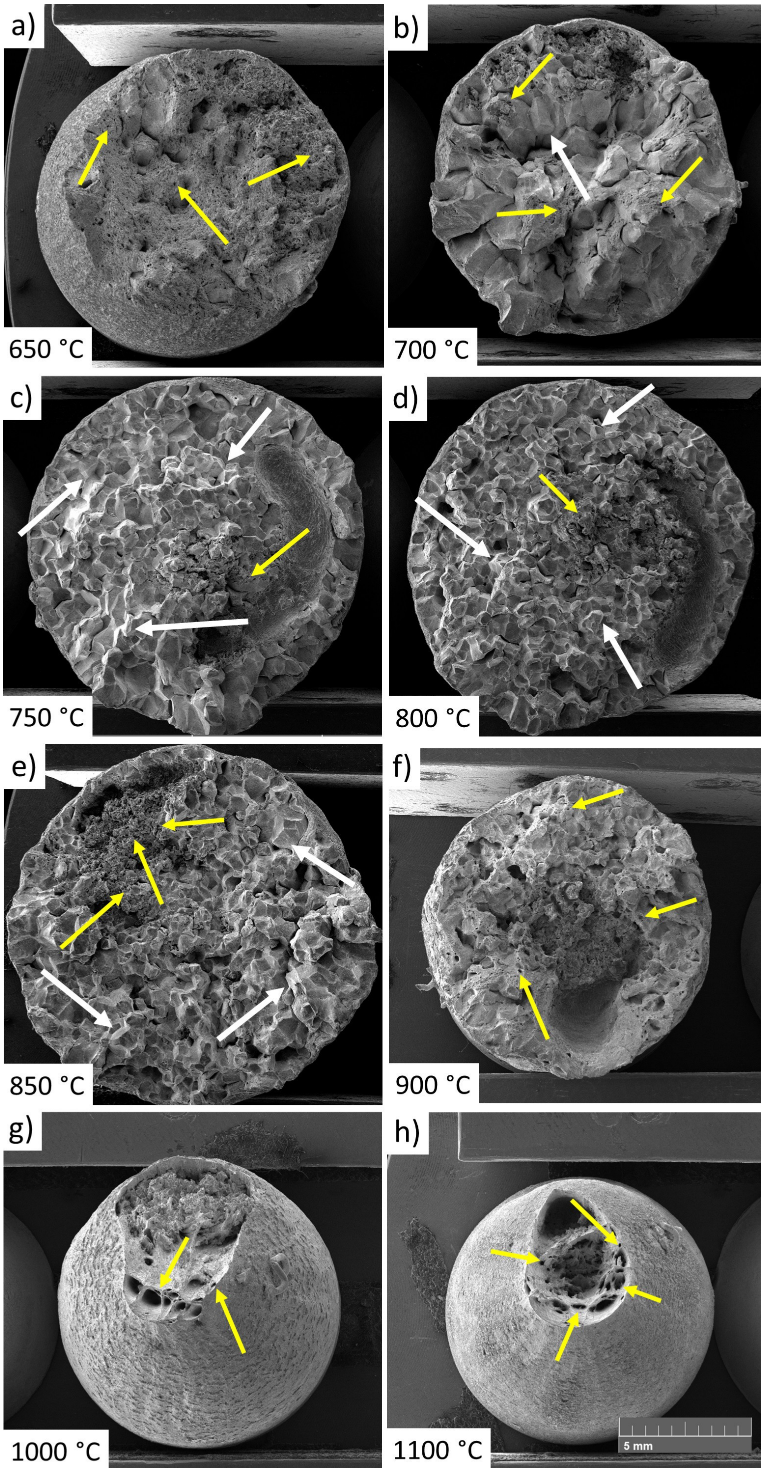

FIGURE 5 Scanning electron microscopy images of samples subjected to tensile test to rupture at a strain rate of $10^{-3}\ s^{-1}$ at different temperatures. The scale bar represents 5 mm.

Figure 5f–h. Furthermore, no intergranular fracture was observed at elevated temperatures.

The scanning electron microscopy images comparing the fracture surfaces of specimens strained at two different strain rates: $10^{-2}\,s^{-1}$ and $10^{-3}\,s^{-1}$, show the ductility minimum temperature for each strain rate, i.e. 750 °C and 800 °C for strain rate of $10^{-2}\,s^{-1}$ and $10^{-3}\,s^{-1}$, respectively as indicated in reduction in area graph, Figure 6. Additionally, two specimens strained at low (650 °C), and high (1100 °C) temperatures are also shown. The micrographs reveal that at the slower strain rate, the fracture surface contains grain facets (indicated by white arrows) and dimples (indicated by yellow arrows), Figure 6d. At the higher strain rate, the fracture surface is covered by dimples with no signs of facets or intergranular cracks, suggesting higher ductility at this strain rate, Figure 6a. At the temperatures where ductility minimum was detected, a well-defined grain structure is observed for both strain rates, Figure 6b, e. At elevated temperatures, both strain rates depict ductile fracture, indicated by dimples throughout the fracture surface suggesting nearly similar ductility, Figure 6c, f.

The evolution of microstructures of the light optical microscopy images of the fracture surface of the specimens strained at different temperatures under a strain rate of $10^{-3}\,s^{-1}$ indicates the formation of ferrite at austenite grain boundaries at lower temperature, Figure 7. Ferrite volume fraction as well as its thickness increases with higher undercooling, i.e., lower temperatures. In this temperature range known as high ductility low temperature zone the smooth fracture surfaces covered by ferrite phase were observed, yellow arrows in Figure 7a. In the critical temperature range of the ductility trough, known as low ductility intermediate temperature zone, the fracture area shows brittle behavior characterized by sharp cracks at grain boundaries (indicated by red arrows). Within this region intergranular brittle fracture is the dominant fracture mechanism, Figure 7b–e. At elevated temperatures known as high ductility high temperature zone, the damaged area shows curved fractures implying ductile fracture, Figure 7f–h. Within both high ductility low temperature and high ductility high temperature regions voids formation, and their coalescence are the predominant fracture mechanism, and as already discussed earlier, no signs of intergranular fracture and crack formation at austenite grain boundaries were observed. Comparing intermediate (700 °C-850 °C) and low temperature (<700 °C) ranges, the fracture mode changes from brittle to ductile due to increased ferrite thickness at austenite grain boundaries. These findings suggest that the ferrite thickness plays a significant role in determining the fracture mechanism.

The micrographs of the light optical microscopy images of the specimens deformed in low ductility intermediate temperature regions at both strain rates reveal that the thickness of ferrite increases with increasing the undercooling which serves as driving force for ferrite nucleation, Figure 8. Moreover, faster deformation reduces the thickness of ferrite at grain boundaries due to less available time for ferrite formation.

The microstructures show that the fracture mode is mostly brittle within this temperature range. The cavitation in the failure area at 700 °C and the strain rate of $10^{-2}\,s^{-1}$ was observed, suggesting ductile fracture at this condition which is reflected in improved ductility (> 40 %) as shown in reduction in area curves, Figure 8a. It

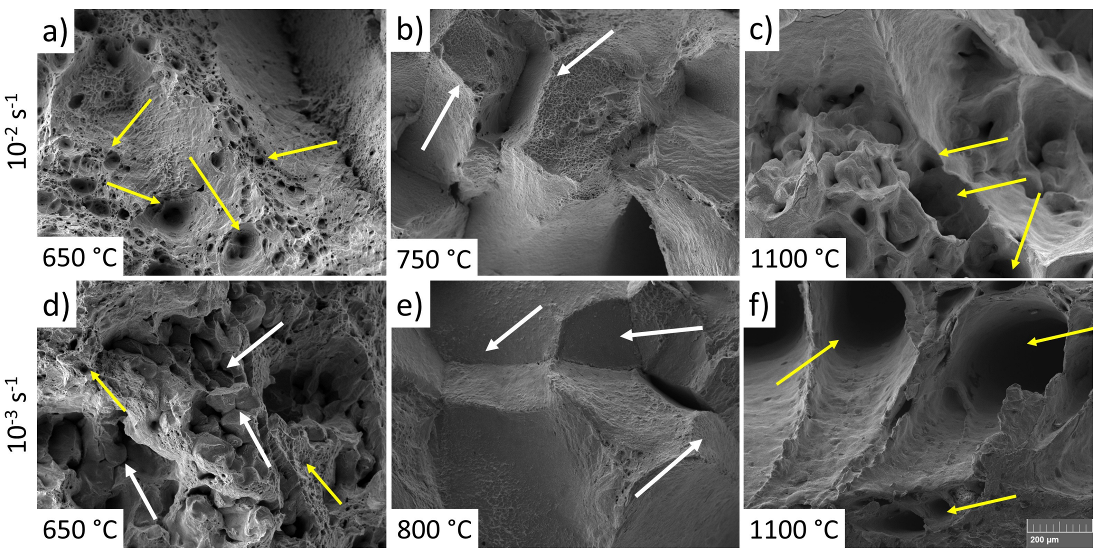

FIGURE 6 Scanning electron microscopy images of samples strained to fracture at different temperatures at the strain rate of a–c) $10^{-2}\,s^{-1}$ and d–f) $10^{-3}\,s^{-1}$. The scale bar represents 200 µm.

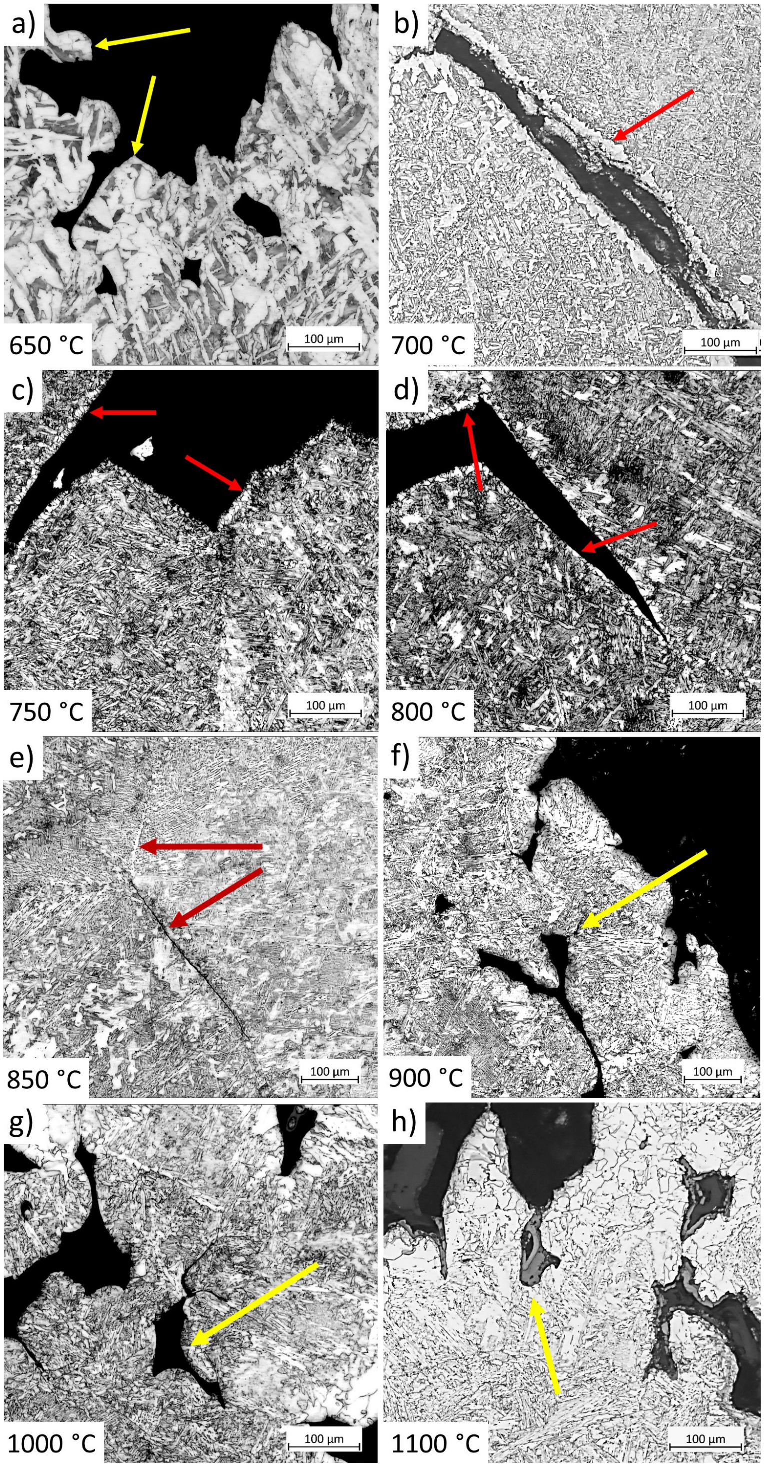

FIGURE 7 Light optical microscopy images of samples subjected to tensile test to rupture at a strain rate of 10^{-3} s^{-1} at different temperatures. The scale bar represents 100 μm.

is interesting to note that cracks mostly propagate along the ferrite/austenite interface under fast deformation, 10^{-2} s^{-1}, white arrows in Figure 8a–b. The fracture occurs within the ferrite during slow deformation, 10^{-3} s^{-1}, black arrows in Figure 8c–e.

In the images of substructures within two microstructures deformed at 700 °C at two strain rates of 10^{-2} s^{-1} and 10^{-3} s^{-1} a well-defined substructure in ferrite within the sample deformed at lower strain rates, 10^{-3} s^{-1}, can be observed, Figure 9. Thus implying the occurrence of dynamic recovery, Figure 9b. No substructure was detected for the ferrite deformed at the higher strain rate, 10^{-2} s^{-1}, Figure 9a.

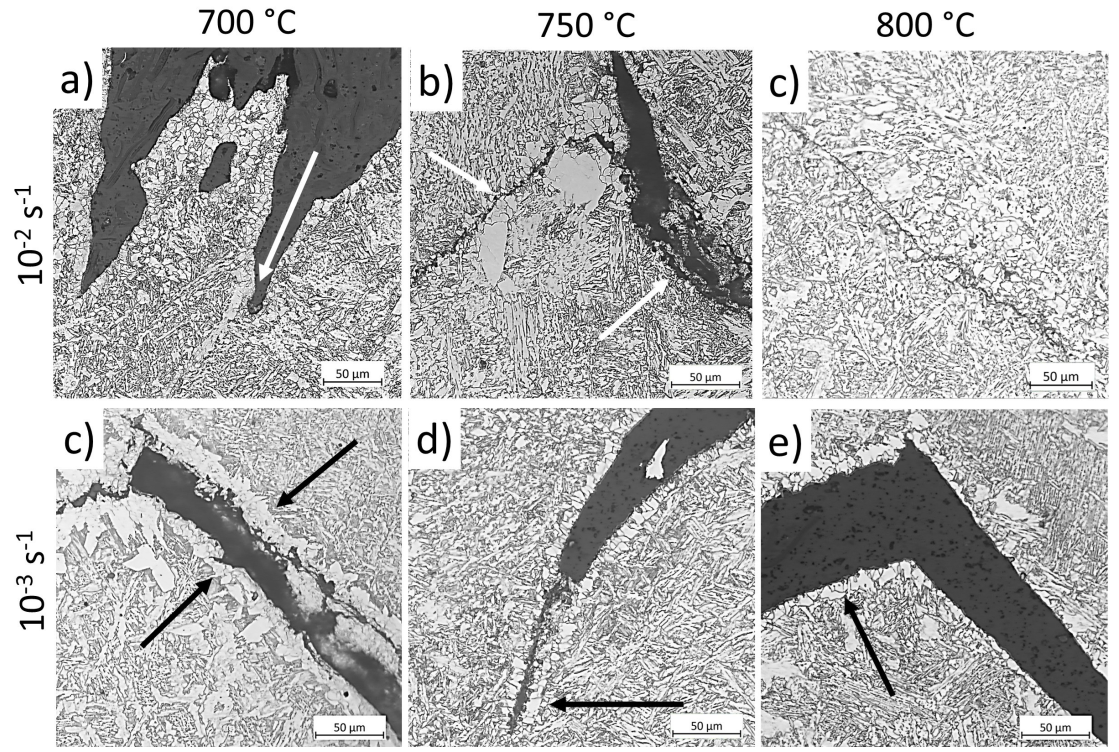

FIGURE 8 The thickness of ferrite film within microstructures subjected to tensile test to rupture at strain rates of $10^{-2}\,s^{-1}$ and $10^{-3}\,s^{-1}$ at different temperatures in low ductility intermediate temperature region. The scale bar represents 50 μm.

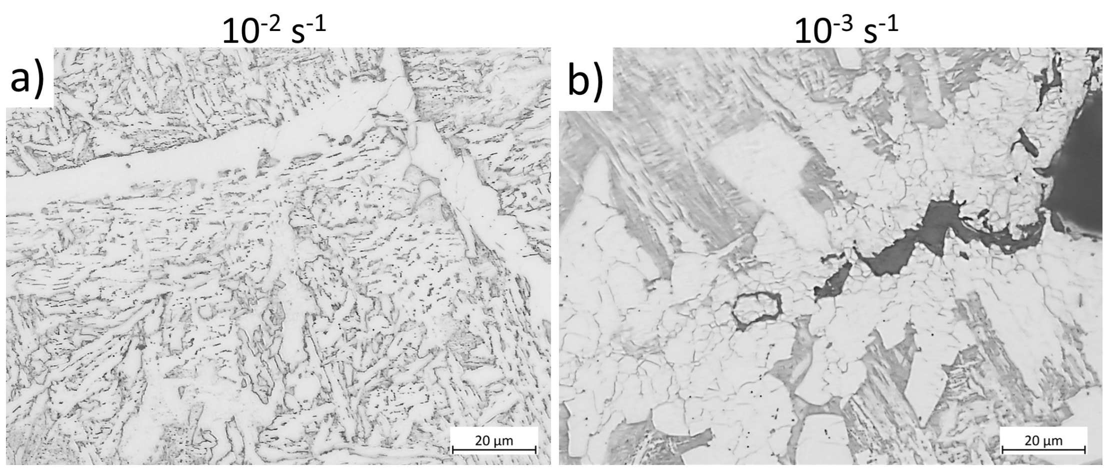

FIGURE 9 Ferrite substructure within samples subjected to tensile test to rupture at 700 °C strain rates of a) $10^{-2}\,s^{-1}$, and b) $10^{-3}\,s^{-1}$. The scale bar represents 20 μm.

The average thickness of ferrite films at grain boundaries for the specimens deformed at various temperatures under two strain rates show that the thickness of ferrite film decreases with increasing temperature, Figure 10. Moreover, ferrite films are thicker under slow deformation conditions. According to measured reduction in area and ferrite thickness at austenite grain boundaries, the critical ferrite film thickness, under which the second ductility minimum occurs, is approximately 8 μm and 18 μm at two strain rates of $10^{-2}\,s^{-1}$ and $10^{-3}\,s^{-1}$, respectively.

4 | DISCUSSION

This study investigates the impact of ferrite film thickness on the ductility of micro-alloyed steel under different thermomechanical conditions. The results reveal a clear relationship between ferrite film thickness, strain

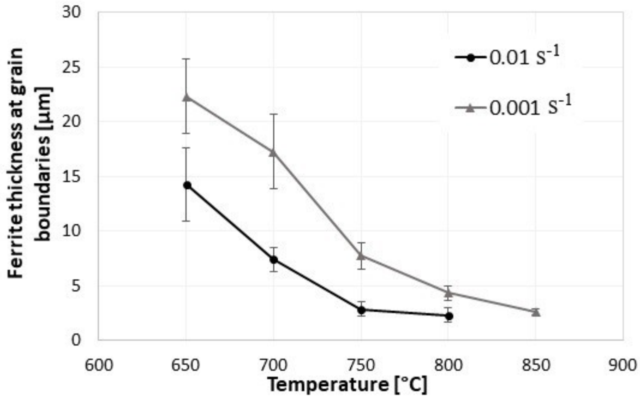

FIGURE 10 Ferrite thickness at grain boundaries at different thermomechanical conditions.

rate, and ductility, providing insights into the material's behavior during continuous casting.

4.1 | The influence of thermomechanical conditions on the ductility

The results demonstrate that both temperature and strain rate significantly influence the ductility of the material. At high ductility high temperature region, the ductility improves with increasing temperature. At 850 °C in the single-phase domain (high ductility high temperature region), the fracture surface comprises ductile fracture identified by microvoid coalescence and dimples, yellow arrows in Figure 5e. Brittle fracture is characterized by intergranular fracture and sharp grain facets, white arrows in Figure 5e. The brittle fracture under this condition is attributed to the rapid dislocation generation, i. e., work hardening of austenite, which promotes crack formation at grain boundaries, leading to brittle cleavage fracture. Higher temperatures within this domain enhance the occurrence of the dynamic recrystallization of austenite, which consumes the deformation energy and reduces the dislocation density by nucleating new grains, which contain lower dislocation density, improving the ductility, Figure 4. However, while a higher strain rate inhibits dynamic recrystallization, ductility improves because there is less time for grain boundary sliding during rapid deformation. Furthermore, within the two-phase domain, the thermomechanical factors, strain rate and temperature, can impact the fracture behavior in two ways: i) altering the microstructure during dynamic austenite to ferrite transformation, and ii) changing the deformation behavior of phases.

4.1.1 | Influence of ferrite film

Ferrite serves as the nucleation site for damage in the two-phase domain due to strain concentration in this softer phase. However, the current study shows that decreasing the temperature increases the thickness of ferrite films by increasing the undercooling which provides the driving force for ferrite nucleation. As ferrite increases, the strain distributes within this phase, reducing strain concentration, and thereby improving the ductility. Therefore, at a given strain rate, the fracture mode changes from brittle fracture identified by sharp cracks at boundaries in the low ductility intermediate temperature region (700 °C–850 °C) to ductile fracture characterized by microvoid and dimples in the high ductility low temperature region (< 700 °C), Figure 6a–d.

4.1.2 | Influence of deformation behavior

Comparing measured reduction in area and ferrite thickness at austenite grain boundaries, it is expected that decreasing the temperature increases the thickness of the ferrite, improving the ductility. However, at a given temperature, thicker ferrite film at the strain rate of $10^{-3}\,s^{-1}$ shows lower ductility than that of $10^{-2}\,s^{-1}$. The lower ductility under lower strain rates is attributed to the deformation behavior of ferrite. Lower strain rates enhance dynamic recovery characterized by a well-defined substructure, softening ferrite phase, Figure 9b, whereas higher strain rates promote work hardening in ferrite. Therefore, under fast deformation, the strength of ferrite increases, allowing it to accommodate more deformation before fracture. This prolongs the time for ferrite formation, enabling strain to distribute more uniformly within the newly formed ferrite, and hence, reducing strain concentration in this phase. Under such conditions, cracks propagate along the ferrite and austenite interface rather than within the soft phase, ferrite, Figure 8b, d. Similar findings were reported during the hot tensile test of low carbon steel [28].

5 | CONCLUSIONS

This study highlights the significant influence of the deformation speed and ferrite phase evolution on the second ductility minimum and provides an insight into the hot ductility behavior of micro-alloyed steel during continuous casting. The research employs hot tensile testing with strain rates of $10^{-2}\,s^{-1}$ and $10^{-3}\,s^{-1}$ within the temperature range of 650 °C–1100 °C. The results lead to the following conclusions:

1. At elevated temperatures within the high ductility high temperature region, ductility improves with increasing temperature due to enhanced dynamic recrystallization of austenite. However, dynamic recrystallization improves the ductility if it is advanced enough to impede void formation and/or grain boundary sliding.
2. Excessive grain boundary sliding, for instance at a very slow deformation, makes dynamic recrystallization less effective in improving the ductility.
3. In the two-phase domain, both temperature and strain rate influence the ductility through two ways, including altering the microstructure during dynamic transformation of austenite to ferrite and changing the deformation behavior of phases.
4. In the two-phase domain, fracture mode transitions from brittle at higher temperatures (700 °C–850 °C) to ductile at lower temperatures (< 700 °C) due to increased ferrite thickness and hindered dynamic recovery at lower temperatures.
5. Higher strain rates (e.g., $10^{-2}\ s^{-1}$) promote work hardening in ferrite, increasing its strength and allowing it to accommodate more deformation before fracture.
6. Increasing the deformation speed improves the ductility by limiting the available time for grain boundary sliding within the temperature range of 650 °C–1100 °C.

USE OF AI

The authors declare that they use Grammarly Inc. to improve their English writing.

AUTHOR CONTRIBUTIONS

Conceptualization, S.B., S.SH, and C.S.; methodology, S.B. and C.S.; formal analysis, S.B., S.SH, and C.S.; Investigation, S.B; resources S.I and C.S.; data curation, S.B.; writing—original draft preparation, S.B. and S.SH.; writing—review and editing S.B., S.SH, S.I., and C.S.; visualization, S.B; supervision C.S.; project administration S.B, S.I., and C.S.; funding acquisition S.I. and C.S. All authors have read and agreed to the published version of the manuscript.

ACKNOWLEDGMENTS

The authors gratefully acknowledge the funding support of K1-MET GmbH, metallurgical competence center. The research program of the K1-MET competence center is supported by COMET (Competence Center for Excellent Technologies), the Austrian program for competence centers. COMET is funded by the Federal Ministry for Climate Action, Environment, Energy, Mobility, Innovation and Technology, the Federal Ministry for Labor and Economy, the Federal States of Upper Austria, Tyrol and Styria as well as the Styrian Business Promotion Agency (SFG) and the Standortagentur Tyrol. Furthermore, Upper Austrian Research GmbH continuously supports K1-MET. Beside the public funding from COMET, this research project is partially financed by the scientific partner Graz University of Technology and the industrial partner voestalpine Stahl GmbH. Additionally, the authors would like to extend their gratitude to Dr. techn. Fernando Gustavo Warchomicka for his assistance with SEM imaging. Austrian funded COMET program (Competence Center Program) K1-MET, funding contract no. FO999892415. Open access funding provided by Technische Universitat Graz/ KEMÖ.

CONFLICT OF INTERESTS STATEMENT

No potential conflict of interest was reported by the author(s).

DATA AVAILABILITY STATEMENT

Data will be made available on request.

ORCID

S. Bakhtiari http://orcid.org/0009-0006-0622-0508

REFERENCES

1. World Steel Assoc. **2024**.
2. X. Jiang, X. M. Chen, S. H. Song, Y. J. Shangguan, *Mater Sci Eng: A* **2013**, *574*, 46.
3. W. Lankford, *Metall Soc AIME* **1972**, *3*, 1331.
4. J. K. Brimacombe, K. Sorimachi, *Metall Trans B* **1977**, *8B*, 489.
5. B. Mintz, S. Yue, J. Jonas, *Int Mater Rev* **1991**, *36*, 187.
6. M. Schöbel, S. Großeiber, J. Jonke, R. Wimpory, S. Ilie, G. Requena, *BHM Berg- Hüttenmänn Mon* **2013**, *158*, 475.
7. B. Mintz, R. Abushosha, *Mater Sci Technol* **1992**, *8*, 171.
8. B. Mintz, J. M. Arrowsmith, *Metals Technol* **1979**.
9. M. M. Arıkan, *Metals (Basel)* **2015**, *5*, 986.
10. O. Caliskanoglu, *Ph.D. Thesis*, Graz University of Technology, Graz, Austria, **2015**.
11. B. Mintz, *Mater Sci Technol* **1996**, *12*, 132.
12. C. Bernhard, J. Reiter, H. Presslinger, *Metall Mater Trans B: Process Metallurgy and Materials Processing Science* **2008**, *39*, 885.
13. B. Mintz, D. N. Crowther, *Int Mater Rev* **2010**, *55*, 168.
14. R. Abushosha, S. Ayyad, B. Mintz, *Mater Sci Technol* **1998**, *14*, 346.
15. D. N. Crowther, Z. Mohamed, B. Mintz, *Trans ISIJ* **1987**, *27*, 366.
16. J. Lewis, J. Jonas, B. Mintz, *ISIJ Int* **1998**, *38*, 300.
17. Y. Maehara, K. Yasumoto, H. Tomono, T. Nagamichi, Y. Ohmori, *Mater Sci Technol (United Kingdom)* **1990**, *6*, 793.
18. B. G. Thomas, I. V. Samarasekera, *ISS Trans* **1986**, *7*, 7.

19. C. Hoflehner, S. Ilie, J. Six, C. Beal, C. Sommitsch, *J Mater Eng Perform* **2018**, *27*, 5124.
20. C. Béal, O. Caliskanoglu, C. Sommitsch, S. Ilie, J. Six, M. Dománková, *Mater Sci Forum* Trans Tech Publications Ltd, **2017**, *pp.* 199.
21. T. N. Baker, *Ironmaking and Steelmaking* **2016**, *43*, 264.
22. K. M. Banks, A. Tuling, B. Mintz, *Mater Sci Technol* **2012**, *28*, 536.
23. K. M. Banks, A. S. Tuling, B. Mintz, *Int J Metall Eng* **2013**, *188*.
24. D. N. Crowther, Z. Mohamed, B. Mintz, *Metall Trans A* **1987**, *18 A*, 1929.
25. M. Gontijo, C. Hoflehner, P. Estermann, S. Ilie, J. Six, C. Sommitsch, *Steel Res Int* **2020**, *91*, DOI 10.1002/srin.202000222.
26. J. Lewisjohn, J. Jonas, B. Mintz, *ISIJ Int* **1997**, *38*, 300.
27. Y. Liu, L. X. Du, H. Y. Wu, R. D. K. Misra, *Steel Res Int* **2020**, *91*.
28. B. Mintz, J. J. Jonas, *Mater Sci Technol* **1994**, *10*, 721.
29. B. Mintz, A. Cowley, R. Abushosha, D. N. Crowther, *Mater Sci Technol* **1999**, *15*, 1179.
30. S. S. Sharifi, R. H. Buzolin, S. Bakhtiari, M. Gontijo, C. Sommitsch, M. C. Poletti, in *J Phys Conf Ser*, Institute of Physics, **2023**.

How to cite this article: S. Bakhtiari, S. S. Sharifi, S. Ilie, C. Sommitsch, *Materialwiss. Werkstofftech.* **2025**, *56*, e202400249. https://doi.org/10.1002/mawe.202400249